HHS Public Access

Author manuscript

Mult Scler. Author manuscript; available in PMC 2020 August 07.

Published in final edited form as:

Mult Scler. ; : 1352458518822408. doi:10.1177/1352458518822408.

The spectrum of spinal cord lesions in a primate model of multiple sclerosis

Jennifer A. Lefeuvre[1,2], **Joseph R. Guy**[1], **Nicholas J. Luciano**[1], **Seung-Kwon Ha**[1], **Emily Leibovitch**[3], **Mathieu D. Santin**[2], **Afonso C. Silva**[4], **Steven Jacobson**[1], **Stéphane Lehéricy**[2], **Daniel S. Reich**[1], **Pascal Sati**[1]

[1]Translational Neuroradiology Section, National Institute of Neurological Disorders and Stroke, National Institutes of Health, Bethesda, Maryland, United States

[2]Institut du Cerveau et de la Moelle – ICM, Centre de NeuroImagerie de Recherche – CENIR, Sorbonne Universités, UPMC Univ Paris 06, UMR S 1127, CNRS UMR 7225, F-75013, Paris, France

[3]Viral Immunology Section, National Institute of Neurological Disorders and Stroke, National Institutes of Health, Bethesda, Maryland, United States

[4]Cerebral Microcirculation Section, Laboratory of Functional and Molecular Imaging, National Institute of Neurological Disorders and Stroke, National Institutes of Health, Bethesda, Maryland, United States

Abstract

Background: Experimental autoimmune encephalomyelitis (EAE) in the common marmoset is a nonhuman primate model of multiple sclerosis (MS) that shares numerous clinical, radiological, and pathological features with MS. Among the clinical features are motor and sensory deficits that are highly suggestive of spinal cord (SC) damage.

Objective: To characterize the extent and nature of SC damage in symptomatic marmosets with EAE using a combined magnetic resonance imaging (MRI) and histopathology approach.

Materials and Methods: SC tissues from five animals were scanned using 7-tesla MRI to collect high-resolution *ex vivo* images. Lesions were segmented and classified based on shape, size, and distribution along the SC. Tissues were processed for histopathological characterization (myelin and microglia/macrophages). Statistical analysis, using linear mixed-effects models, evaluated the association between MRI and histopathology.

Results: Marmosets with EAE displayed two types of SC lesions: focal and subpial lesions. Both lesion types were heterogeneous in size and configuration, and corresponded to areas of marked demyelination with high density of inflammatory cells. Inside the lesions, the MRI signal was significantly correlated with myelin content ($p<0.001$).

Correspondence should be addressed to: Dr. Pascal Sati, Translational Neuroradiology Section/NINDS/NIH, 10 Center Drive MSC 1400, Building 10 Room 5C103, Bethesda, MD 20852, USA. Phone number: +1-301-402-1436; satip@ninds.nih.gov.

Declaration of conflicting interest

J.A.L, J.R.G, N.J.L., S.K.H., E.L., M.D.S, A.C.S., S.J., S.L, D.S.R, P.S, declared no potential conflicts of interest with respect to the research, authorship, and/or publication of this article.

Conclusion: Our findings underscore the relevance of this nonhuman primate EAE model for better understanding mechanisms of MS lesion formation in the SC.

Keywords

Multiple sclerosis; Spinal cord; EAE; MRI; Marmoset

Introduction

Experimental autoimmune encephalomyelitis (EAE) is the most commonly used animal model for studying multiple sclerosis (MS)[1,2]. While mouse EAE models are a vital component of preclinical research in MS, the marmoset EAE model has recently gained some attention due to marmosets' closer genetic and immunological proximity to humans[3,4]. This nonhuman primate model of MS also bears strong pathological and radiological similarities to MS,[5] while still maintaining practicality as a model, making it an excellent system for studying the mechanisms of lesion formation in the brain[6].

Among the various clinical symptoms experienced by marmosets with EAE, motor and sensory deficits are often present, which strongly suggest the presence of demyelinated lesions in the spinal cord (SC). A few histopathological studies have reported the presence of pathology in SC tissues from marmosets with EAE[3,7,8,9,10]. However, these studies did not characterize in a comprehensive manner the extent of the SC pathology.

Magnetic resonance imaging (MRI) is a noninvasive and sensitive tool for detecting pathology in the central nervous system (CNS). However, MRI of the SC is challenging, especially in small animals like the common marmoset, due to the extremely small dimensions of the cord. Therefore, we investigated the spinal cord pathology by postmortem MRI, where high signal-to-noise ratio can be obtained to produce high-quality and high-resolution images. These *ex vivo* MRI images can then be used to guide precisely any subsequent tissue sampling for histology, and to evaluate pathologically specific areas of the CNS affected by EAE[12].

In this study, we used an experimental approach combining *ex vivo* MRI with histopathology, with the goal of characterizing the extent and nature of the pathology affecting the SC in the marmoset model of MS.

Materials and Methods

EAE induction

All common marmosets (*Callithrix jacchus*) used in this study were housed at the NIH Intramural Research facilities, in accordance with the standards of the American Association for Accreditation of Laboratory Animal Care and the NINDS Animal Care and Use Committee. Five adult marmosets [mean age 3.5 years (range: 1.5–4.9), 4 females] were included in this study. Four animals were induced with EAE using white matter homogenate in complete Freund's adjuvant[13] which in our hands produces a disease that bears strong radiological similarities to MS[5]. The fifth animal was used as a healthy, non-EAE control. Animals were frequently weighed and scored according to an EAE scale based on clinical

symptoms[14]. Table 1 provides the demographics and clinical summary of these animals. Once the animals showed paraplegia and/or 20% weight loss, the experiment was terminated by performing transcardial perfusion fixation with cold 4% paraformaldehyde under anesthesia. The spine was removed and stored in 4% neutral buffered formalin.

MRI acquisition

After extraction and preparation of the SC samples (see supplementary Figure 1), MRI was performed on a 7T/30 cm MRI scanner (Bruker BioSpin Corp., Ettlingen, Germany) equipped with a 15 cm gradient set of 450 mT/m strength (Resonance Research Inc., Billerica, MA, USA). A proton-only transmit-receive volume coil (25 mm inner diameter) (Bruker) was used for imaging the tissue samples loaded in the plastic tubes. During each scanning session, a 3-dimensional (3D) T_2*-weighted gradient-echo sequence with an in-plane resolution of 70 μm and a slice thickness of 200 μm was acquired 4 times consecutively for a total acquisition time of 12 hours (see Supplementary Table 1 for acquisition parameters).

Image analysis

All four acquisitions were first averaged using the MIPAV image analysis software (National Institutes of Health, Bethesda, Maryland; http://mipav.cit.nih.gov). After a N4-bias-field correction[15] was applied to correct for intensity inhomogeneity, images were upsampled to an in-plane axial resolution of 35 μm × 35 μm and a 70 μm slice thickness and concatenated to generate a single image volume of the entire SC using ImageJ software (National Institutes of Health, Bethesda, Maryland; https://imagej.nih.gov/ij/) and MIPAV. Finally, the different spinal level segments were annotated based on the location of the nerve roots[16].

Focal lesions (areas of abnormal signal intensity within the white matter (WM)) were manually segmented (ITK-SNAP version 3.2.0) using triplanar viewing mode. Lesions were classified according to their volume using the following arbitrary categories: small (0.009-0.06 mm^3), medium (0.06-0.4 mm^3), and large (>0.4 mm^3). The specific position of the focal lesions was also recorded as anterior, posterior, and lateral (left/right). Subpial lesions were also manually segmented on select images at three different levels of the cord (C7, T7, and L3). Regions-of-interest (ROIs) of the entire cross-sectional cord, normal appearing white matter (NAWM), and gray matter (GM) were drawn manually (Supplementary Figure 2) using a semi-automated tool in JIM V.7.0 (Xinapse Systems, Leicester, UK). The relative thickness of subpial lesions (areas of abnormal signal intensity along the edge of the WM) was characterized as a percentage of total WM using the following formula: $\text{Area ROI}_{\text{subpial lesion}} / (\text{Area ROI}_{\text{cross-sectional cord}} - \text{Area ROI}_{\text{GM}}) \times 100$. The degree of severity for the subpial lesions was arbitrarily defined as: low if < 20%; intermediate if between 20–50%; and high if > 50%.

Histopathology

Focal and subpial lesions with various sizes, shapes, and locations identified by *ex vivo* MRI were targeted during the cutting process (transaxial cuts of 3 mm-thick slabs). Slabs from the control animal were selected at similar cord levels for comparison purposes. A total of 32 slabs were cut, and then embedded in paraffin wax. These paraffin-embedded slabs were

sectioned in 5 μm-thick slices to find the lesions detected by MRI. Luxol fast blue with periodic acid-Schiff (LFB-PAS) staining, ionized calcium-binding adapter molecule 1 (Iba-1) immunohistochemistry, and 3,3'-diaminobenzidine (DAB)-enhanced Turnbull staining were performed on a subset of slices containing lesions. Details of the staining protocols are provided in the supplementary material. Digital pictures of the stained slides were generated using a Zeiss Observer 1 microscope (ZEN blue software (Zeiss, Thomwood, NY) at 10× optical zoom with a pixel resolution 0.7 μm, and exported as TIFF files.

MRI-histopathological comparison

A semi-quantitative comparison was performed by selecting 11 different lesions (9 focal and 2 subpial) on MRI and rating their corresponding histological images. A contour line for each lesion was first drawn on each histological image using the following procedure. MRI images were first coregistered to the corresponding LFB-PAS histology images using thin-plate splines with control points initialized manually (MIPAV, NIH). Lesions were then segmented on MRI images by using an intensity level threshold. The corresponding contour line was defined using the ROI tool and propagated to the histological images. The contrast between lesion and GM ($Contrast_{lesion\text{-}to\text{-}GM}$ = $Signal\ intensity_{lesion}$/$Signal\ intensity_{GM}$) was computed and reported for these selected lesions. The level of demyelination inside the contoured lesions was rated on LFB-PAS using the following grading system: 0 = normal myelin density; 1 = reduced myelin density; 2 = completely demyelinated. The level of inflammation was rated on Iba-1 using the following grading system: 0 = absent/few inflammatory cells; 1 = moderate density of inflammatory cells; 2 = high density of inflammatory cells.

A more quantitative comparison between MRI and histopathology was performed using regression models (see "Statistical analysis") on the coregistered *ex vivo* MRI, LFB-PAS, and Iba-1 images. To generate data for fitting the statistical models, a total of 92 ROIs were drawn manually on LFB-PAS images using ImageJ at different cross-sectional cord locations (WM, GM, and lesion) of several sections (8–14 ROIs per section) (Supplementary Figure 3). ROIs were then propagated to the corresponding MRI images and Iba-1 staining. From each staining, the function "color deconvolution" (ImageJ) was applied to extract the channel corresponding to the stain of interest (LFB channel for the myelin component of LFB-PAS and DAB channel for the inflammatory cells of Iba-1). Mean signal intensity for each ROI was computed on both MRI and grayscale-deconvoluted staining images.

Statistical analysis

The nonparametric two-tailed Mann Whitney test (Prism v7.0b) was performed to test any association between the $Contrast_{lesion\text{-}to\text{-}GM}$ values and histopathology scores. To assess the association between MRI and histopathology signals and identify which variables influenced the MRI signal, we performed regression models and evaluated different statistical models, summarized in Table 2. In all models, the independent variable was the histopathology and the dependent variable was the MRI signal intensity. Two linear mixed-effects models (M_1 and M_2) were used with random effect of section, to account for the correlated observations taken from the same section. A simple linear model M_0 was run for completeness. M_2, the

most complex model, included an interaction term to test the hypothesis that the relationship between MRI and pathology depends on the tissue type (NAWM, GM, lesions). We evaluated these different regression models for both LFB (called the myelin model) and Iba-1 (called the inflammation model) by comparing their Akaike Information Criteria (AIC)[17] values; the best model was considered to have the lowest AIC value. Because AIC values are ordinal and give a rank of the model goodness-of-fit, the ΔAIC values were reported as well: $\Delta AIC(n) = AIC(n) - AIC_{min}$ where n denotes the model of interest and AIC_{min} the minimum AIC of all the models tested. Regression results were considered significant for $p \leq 0.05$. The coefficient of determination, R^2, was reported to evaluate the goodness-of-fit using the method of Nakagawa et al. adapted for the linear mixed-effects models[18]. Statistical analysis and graphical visualization were performed using R version 3.3.3 and Rstudio (1.0.143). The lme4 package version 1.1-16 was used to fit the mixed-effects model using restricted maximum likelihood estimation.

Results

All immunized animals developed clinical signs between 65 and 100 days post-immunization and reached EAE scores ≥2.5 at the time of sacrifice. Disease duration (from immunization to death) ranged from 71 to 159 days (mean: 113 days) (Table 1). All four EAE animals displayed SC abnormalities on postmortem MRI images (Figure 1). Focal WM lesions with various sizes and shapes were observed at different cord levels (Figure 1, red arrows). A total of 85 focal WM lesions were segmented on the MRI images across the four EAE animals. Thirty-four lesions (40%) were found at the cervical level, 40 (47%) at the thoracic level, and 11 (13%) at the lumbar level (Table 3). Fifty-seven lesions (67%) were classified as small (average volume: 0.028 mm^3), 24 lesions (28%) as medium-sized (0.11 mm^3), and 4 lesions (5%) as large (2.54 mm^3) (Table 3). Sixty-nine focal WM lesions (81%) were located in the lateral WM, fifteen lesions (18%) were located in the posterior WM, and only 1 lesion was found in the anterior WM (Table 3). Subpial WM lesions were also observed along the entire cord, with variable thickness (Figure 1, green arrows). Three animals (M#1, M#2, and M#3) displayed thin subpial WM lesions (relative thickness <21%) throughout their entire cords, whereas one animal (M#4) showed thicker subpial WM lesions (relative thickness >39%) in the lumbar portion of the cord (Table 4).

Anatomical features observed on MRI were visually matched on histological sections in control and EAE animals (Figure 2). In the control animal, both MRI and histology depicted normal WM with dark gray (denoted here as “isointense”) MRI signal (Figure $2A_1$), normal LFB staining (Figure $2B_1$), and absence of “reactive” inflammatory cells on Iba-1 (Figure $2C_1$). In the EAE animals, focal and subpial WM cord lesions detected as areas of hyperintense MRI signal (Figure $2A_2$-A_4) corresponded to areas of clear demyelination characterized by low LFB (Figure $2B_2$-B_4) staining, as well as intense inflammation demonstrated by strong Iba-1 staining (Figure $2C_2$-C_4).

The semi-quantitative analysis performed on a subset of 11 lesions revealed heterogeneity in myelin content and density of inflammation (Supplementary Table 2). This heterogeneity is illustrated by representative examples of a completely demyelinated lesion (Figure $3A_{2\text{-}3}$) with intense inflammation (Figure $3A_4$) and a partially demyelinated lesion (Figure $3B_{2\text{-}3}$)

with moderate inflammation (Figure $3B_4$). The semi-quantitative analysis also indicated an association between MRI signal and myelin content/density of inflammatory cells (Supplementary Table 2). Completely demyelinated lesions (score = 2) showed a significantly higher $Contrast_{lesion\text{-}to\text{-}GM}$ value than lesions with partial demyelination (score = 1) (Figure 4). A similar trend was observed when comparing lesions with high density of Iba-1 cells (score = 2) against lesions with a moderate density of cells (score = 1), although the difference in $Contrast_{lesion\text{-}to\text{-}GM}$ values was not significant in this case (Figure 4).

The quantitative analysis performed on the individual 92 ROIs revealed a lower AIC value when an interaction term for tissue type and random effect for sections were added in the myelin model (M_2) (see Table 2). Figure 5 illustrates the importance of the random effect when predicting MRI values. In the M_2 regression model, R^2 of 0.96 indicated that 96% of the variability in the MRI data were explained by the predictors (fixed and random effects) in this model (Supplementary Figure 5). P-values and mean slope coefficients from the linear mixed-effects model M_2 are summarized in Supplementary Table 3. Significant and strong positive associations were found between LFB and MRI values for both lesional and GM tissues. No significant association was seen between the LFB and MRI values in the NAWM, but the variation in MRI signal intensity within NAWM was comparatively small. A negligible difference in AIC values was observed when adding an interaction term in the inflammation models (Table 2). The lowest AIC value was obtained for M_1, which includes random effects but no interaction term. No significant association was found between the Iba-1 and the MRI signal (slope [standard error] = −10 [10.9], p=0.35).

Discussion

In this study, we investigated the SC pathology in marmosets with EAE using a combined MRI-histopathological approach. By acquiring high-resolution *ex vivo* MRI, we first identified two types of lesions: (1) focal lesions located within the WM of the SC, (2) subpial lesions along the WM abutting the subarachnoid space. By comparing our *ex vivo* MRI images with histology, we then demonstrated that these lesions corresponded to areas of demyelination and marked inflammation.

Similar to focal MS lesions[19,20], focal EAE lesions were found throughout the SC of the marmoset, with a prevalent localization in the lateral and posterior columns. We observed a heterogeneous distribution in terms of number and size of the focal lesions, which is also consistent with the lesion heterogeneity described in MS patients[21]. To our knowledge, only one histopathological study has reported the presence of diffuse subpial demyelination[22]. In our model, subpial EAE lesions were distributed throughout the animal cords and showed variable thicknesses between animals. Note that these subpial lesions were difficult to visualize by postmortem MRI without performing first a laminectomy. Indeed, the tissues (bones, fat, and muscles) surrounding the SC generated magnetic susceptibility-related artifacts that hid these subtle lesions located at the edge of the cord (Supplementary Figure 6). Thus, we hypothesize that the technical issues described above combined with comparatively low resolution MRI might explain why subpial cord lesions have not been yet reported by MRI in MS patients. A recent in vivo imaging study of the cervical cord in MS patients found a decrease in magnetization transfer ratio values for the outermost voxels of

the SC,[23] which could correspond to the subpial pathology observed in our study, but this would need to be verified histopathologically.

For lesion types, our histopathological evaluation revealed variable degrees of demyelination and inflammatory cell densities, which most likely reflects different stages of lesion development, as recently demonstrated for marmoset brain lesions[6]. Note that the small focal inflammatory demyelinated lesions appeared to follow parenchymal blood vessels, whereas the larger subpial inflamed demyelinated lesions detected in our model are consistent with a leptomeningeal inflammatory origin, as is postulated to be the case for subpial cortical lesions[24,25]. Interestingly, meningeal inflammation has already been reported in MS SC[22,26].

By performing a quantitative comparison between MRI and histopathology using regression models, we established a strong association between the (T_2*-weighted) MRI signal intensity and the amount of myelin derived from the LFB-PAS stain intensity level within the GM and lesional areas. By contrast, the association between the MRI signal and the density of inflammatory cells was weaker (Figure 4). The use of a linear mixed-effects model allowed us to improve the prediction of MRI values by correcting for the correlation within section (Figure 5). These results highlight the fact that T_2*-weighted MRI signal can be highly sensitive to demyelination (although not specific) and corroborate previous postmortem studies investigating MRI and its pathological correlates in the MS SC[27].

Important limitations of this study were the use of a single, postmortem timepoint with a single MRI contrast (T_2*-weighted). The postmortem timepoint illuminates the SC lesion load when symptoms are severe (20% weight loss or paraplegia), but cannot provide spatiotemporal context of the pathology. Additionally, because we were not able to scan these spinal cords in vivo, we have no information regarding the age and the blood-brain-barrier integrity of the lesions analyzed here. Both of these processes can play a role in the development of vasogenic edema and expansion of the interstitial space, which can also impact signal intensity on postmortem MRI. Finally, our MRI sequence was optimized to provide the best delineation between lesions and NAWM. Therefore, lesions affecting the GM of the SC could not be easily identified by MRI in this study, although we detected GM pathology by histology in some of our sections (Figures 2 and 3, purple arrows).

Conclusions

In this study, we investigated SC tissues from marmosets with EAE showing symptoms suggestive of SC damage. Using a combined MRI-histopathological approach, we established the existence of two types of WM SC lesions: focal WM lesions with characteristics (location, distribution, and size) overlapping those found in human MS SC, and subpial WM lesions, which so far have not been reported in MS. We found that both focal and subpial EAE lesions detected by MRI corresponded to areas of demyelination and marked inflammation. Our findings underscore the relevance of this nonhuman primate model of MS for understanding mechanisms of lesion formation in the SC. Future work is needed to investigate the existence of SC subpial lesions in MS as well as *in vivo* marmoset SC imaging to unravel the spatiotemporal development of SC pathology.

Supplementary Material

Refer to Web version on PubMed Central for supplementary material.

Acknowledgments

The authors wish to thank Cecil Chern-Chyi Yen who helped with troubleshooting the scanner used in this study; Sam Antonio and James O'Malley in the NIH animal facility for marmoset care and project support; and Gina Norato, NINDS statistician, for her help to apply the linear mixed-effect models.

This research was supported by the Intramural Research Program of the NIH, NINDS. This research was presented in part at the 24th annual meeting of the International Society for Magnetic Resonance in Medicine (Singapore, 2016).

Funding

This research was supported by the Intramural Research Program of the National Institute of Neurological Disorders and Stroke.

Abbreviations:

EAE	experimental autoimmune encephalomyelitis
MS	multiple sclerosis
SC	spinal cord
LFB	Luxol fast blue
Iba-1	ionized calcium-binding adapter molecule 1
7T	7-tesla
T2*w	T2*-weighted

References

1. Baxter AG. The origin and application of experimental autoimmune encephalomyelitis. Nat Rev Immunol. 2007; 7: 904–12. [PubMed: 17917672]
2. Linker RA and Lee DH. Models of autoimmune demyelination in the central nervous system: on the way to translational medicine. Exp Transl Stroke Med. 2009; 1: 5. [PubMed: 20142992]
3. Massacesi L, Genain CP, Lee-Parritz D, et al. Active and passively induced experimental autoimmune encephalomyelitis in common marmosets: a new model for multiple sclerosis. Ann Neurol. 1995; 37: 519–30. [PubMed: 7717689]
4. Kap YS, Laman JD, 't Hart BA. Experimental autoimmune encephalomyelitis in the common marmoset, a bridge between rodent EAE and multiple sclerosis for immunotherapy development. JNeuroimmune Pharmacol. 2010;5(2):220–30. [PubMed: 19826959]
5. Absinta M, Sati P, Reich DS. Advanced MRI and staging of multiple sclerosis lesions. Nat Rev Neurol. 2016;12(6):358–68. [PubMed: 27125632]
6. Maggi P, Macri SM, Gaitan MI, et al. The formation of inflammatory demyelinated lesions in cerebral white matter. Ann Neurol. 2014;76(4):594–608. [PubMed: 25088017]
7. Hart BA, Bauer J, Muller HJ, et al. Histopathological characterization of magnetic resonance imaging-detectable brain white matter lesions in a primate model of multiple sclerosis: a correlative study in the experimental autoimmune encephalomyelitis model in common marmosets (Callithrix jacchus). Am J Pathol. 1998;153(2):649–63. [PubMed: 9708823]

8. 't Hart BA, Massacesi L Clinical, pathological, and immunologic aspects of the multiple sclerosis model in common marmosets (Callithrix jacchus). J Neuropathol Exp Neurol. 2009;68(4):341–55. [PubMed: 19337065]
9. Laman JD, van Meurs M, Schellekens MM, et al. Expression of accessory molecules and cytokines in acute EAE in marmoset monkeys (Callithrix jacchus). J Neuroimmunol. 1998;86(1):30–45. [PubMed: 9655470]
10. Villoslada P, Hauser SL, Bartke I, et al. Human nerve growth factor protects common marmosets against autoimmune encephalomyelitis by switching the balance of T helper cell type 1 and 2 cytokines within the central nervous system. J Exp Med. 2000;191(10):1799–806. [PubMed: 10811872]
11. Stroman PW, Wheeler-Kingshott C, Bacon M, et al. The current state-of-the-art of spinal cord imaging: methods. Neuroimage. 2014;84:1070–81. [PubMed: 23685159]
12. Guy JR, Sati P, Leibovitch E, et al. Custom fit 3D-printed brain holders for comparison of histology with MRI in marmosets. J Neurosci Methods. 2016;257:55–63. [PubMed: 26365332]
13. Lee NJ, Ha SK, Sati P, et al. Spatiotemporal distribution of fibrinogen in marmoset and human inflammatory demyelination. Brain. 2018;141(6):1637–49. [PubMed: 29688408]
14. Kap YS, Smith P, Jagessar SA, et al. Fast progression of recombinant human myelin/oligodendrocyte glycoprotein (MOG)-induced experimental autoimmune encephalomyelitis in marmosets is associated with the activation of MOG34-56-specific cytotoxic T cells. J Immunol. 2008;180(3):1326–37. [PubMed: 18209026]
15. Tustison NJ, Avants BB, Cook PA, et al. N4ITK: improved N3 bias correction. IEEE Trans Med Imaging. 2010;29(6): 1310–1320. [PubMed: 20378467]
16. Watson C, Sengul G, Tanaka I, et al. The spinal cord of the common marmoset (Callithrix jacchus). Neurosci Res. 2015; 93:164–75. [PubMed: 25575643]
17. AKAIKE H (1973). Information theory and an extension of the maximum likelihood principle In 2nd International Symposium on Information Theory, Ed. Petrov BN and Csaki F, pp. 267–81. Budapest: Akademia Kiado.
18. Nakagawa S and Schielzeth H A general and simple method for obtaining R2 from generalized linear mixed-effects models. Methods Ecol Evol, 2013 2 1;4(2):133–42
19. Oppenheimer DR. The cervical cord in multiple sclerosis. Nenropathol Appl Neurobiol. 1978;4(2): 151–162.
20. Weier K, Mazraeh J, Naegelin Y, et al. Biplanar MRI for the assessment of the spinal cord in multiple sclerosis. Mult Scler. 2012; 18(ll):1560–9. [PubMed: 22539086]
21. Nijeholt GJ, Bergers E, Kamphorst W, et al. Post-mortem high-resolution MRI of the spinal cord in multiple sclerosis: a correlative study with conventional MRI, histopathology and clinical phenotype. Brain. 2001;124(Pt 1): 154–166. [PubMed: 11133795]
22. Androdias G, Reynolds R, Chanal M, et al. Meningeal T cells associate with diffuse axonal loss in multiple sclerosis spinal cords. Ann Neurol. 2010;68(4):465–76. [PubMed: 20687208]
23. Kearney H, Yiannakas MC, Samson RS, et al. Investigation of magnetization transfer ratio-derived pial and subpial abnormalities in the multiple sclerosis spinal cord. Brain. 2014;137(Pt 9):2456–2468. [PubMed: 24966048]
24. Reich DS, Lucchinetti CF, Calabresi PA. Multiple Sclerosis. N Engl J Med. 2018;378(2):169–80. [PubMed: 29320652]
25. Choi SR, Howell OW, Carassiti D, Magliozzi R, Gveric D, Muraro PA, et al. Meningeal inflammation plays a role in the pathology of primary progressive multiple sclerosis. Brain. 2012;135(Pt 10):2925–37. [PubMed: 22907116]
26. DeLuca GC, Alterman R, Martin JL, et al. Casting light on multiple sclerosis heterogeneity: the role of HLA-DRB1 on spinal cord pathology. Brain. 2013;136(Pt 4):1025–34. [PubMed: 23485854]
27. Schmierer K, McDowell A, Petrova N, et al. Quantifying multiple sclerosis pathology in post mortem spinal cord using MRI. Neuroimage. 2018.

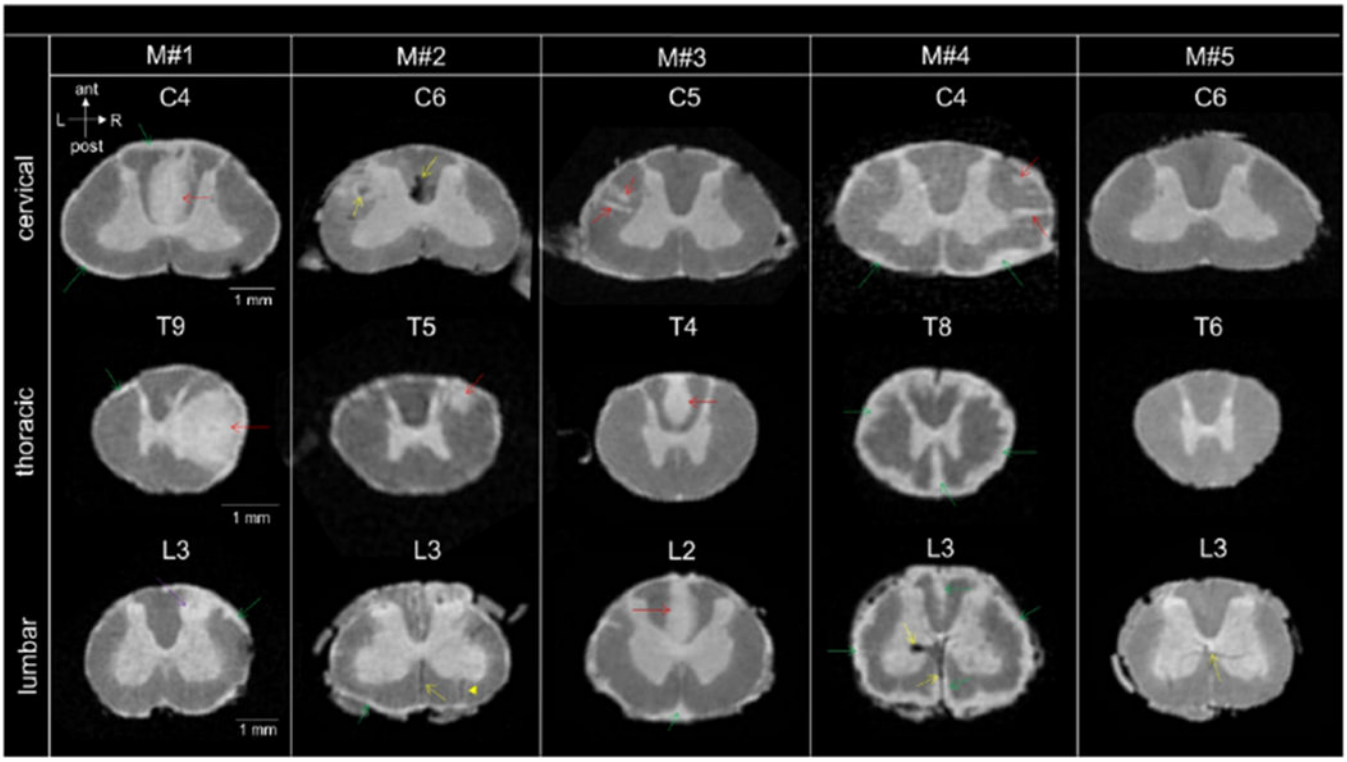

Figure 1.

High-resolution postmortem MRI scans of four marmoset spinal cords with EAE (M#1, M#2, M#3, M#4) and one healthy control (M#5) showing cervical, thoracic, and lumbar spinal cord levels. Anatomical orientation axes are included (white arrows): anterior (ant), posterior (post), left (L) and right (R). The heterogeneity of the focal lesions (red arrows) and subpial lesions (green arrows) in terms of size, shape and location can be observed across the marmosets with EAE. Areas of hypointense signal (yellow arrows) were sometimes observed in these animals (M#2, C6 and M#4, L3), most likely originating from blood deposits (see Supplementary Figure 4). Parenchymal vessels with deoxygenated blood could also be visualized as dark thin lines (yellow dotted arrows, L3 for M#2, M#4 and M#5), sometimes running centrally through a focal lesion (plain yellow arrow, M#2, L3). Note the mass effect produced by a large tumefactive lesion (M#1, T9, red arrow) that involves most of the right lateral column and some of the GM. Another lesion affecting the GM (purple arrow) coud also be found within the dorsal horn at the lumbar level (M#1, L3). Various degree of confluence for the subpial lesions can be appreciated. For three animals (M#1, M#2, M#3), subpial lesions were subtle and not confluent compared to animal M#4 that displayed partially confluent (C4) and completelely confluent at the lower levels of the SC (T8 and L3).

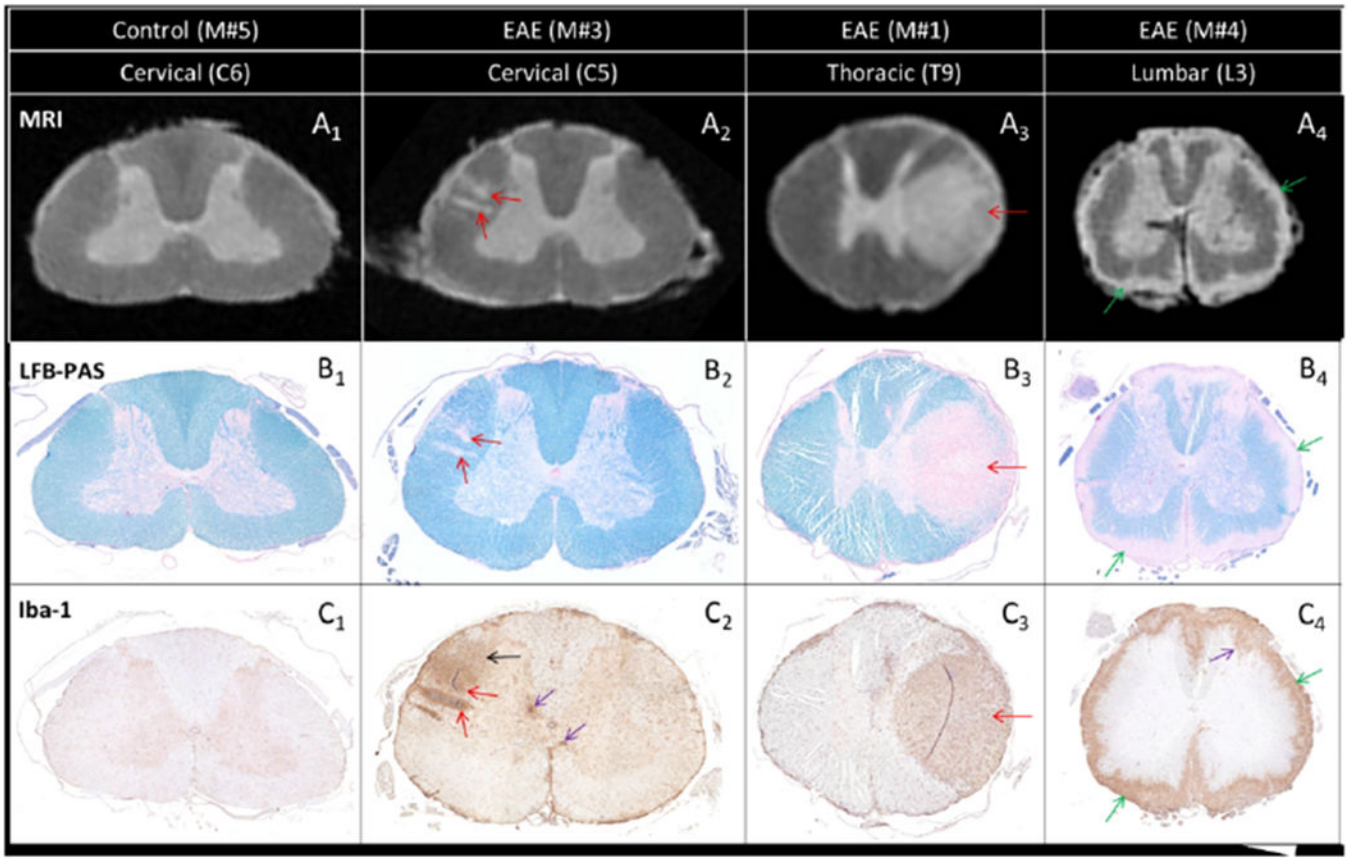

Figure 2.

Comparison between MRI scans (A) and histopathology sections (B and C) from a control animal (M#5) and three EAE animals (M#3, M#1, and M#4). Two small focal lesions detected by MRI in the cervical section (A_2, red arrows) correspond to two small demyelinated areas (B_2, red arrows) with intense inflammatory cell infiltration (C_2, red arrows). Note also the more diffuse inflammatory cell infiltration located above the two lesions, not captured by MRI (C_2, black arrow). The large tumefactive focal lesion detected by MRI in the thoracic section (A_3, red arrow) matches an area of demyelination (B_3, red arrow) and inflammatory cell infiltration (C_3, red arrow). A similar correspondence between MRI and histopathology is observed at the lumbar level (A_4, B_4, C_4) for the subpial lesion (green arrows). Although not visible on the MRI, inflammation can be found within the GM (purple arrows) either infiltrating the dorsal horn (C_4) or seen as small foci (C_2).

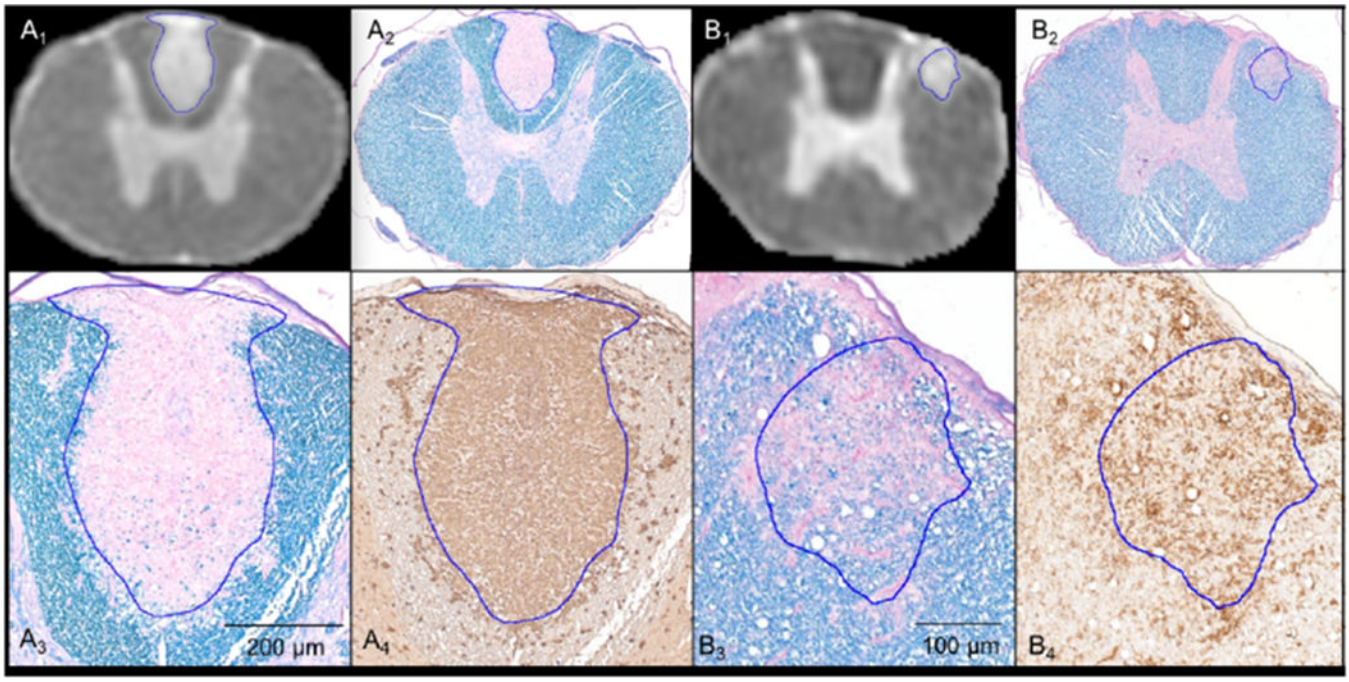

Figure 3.

MRI scans (A_1 and B_1) coregistered to the corresponding LFB-PAS images (A_2 and B_2) for defining the lesion contour ROI (blue lines). Magnified views of the lesions for LFB-PAS (A_3 and B_3) and Iba-1 (A_4 and B_4). A_3 and A_4 show complete myelin loss and uniform intensity of inflammatory cells throughout the entire lesion. B_3 and B_4 show a partially demyelinated lesion with moderate inflammation.

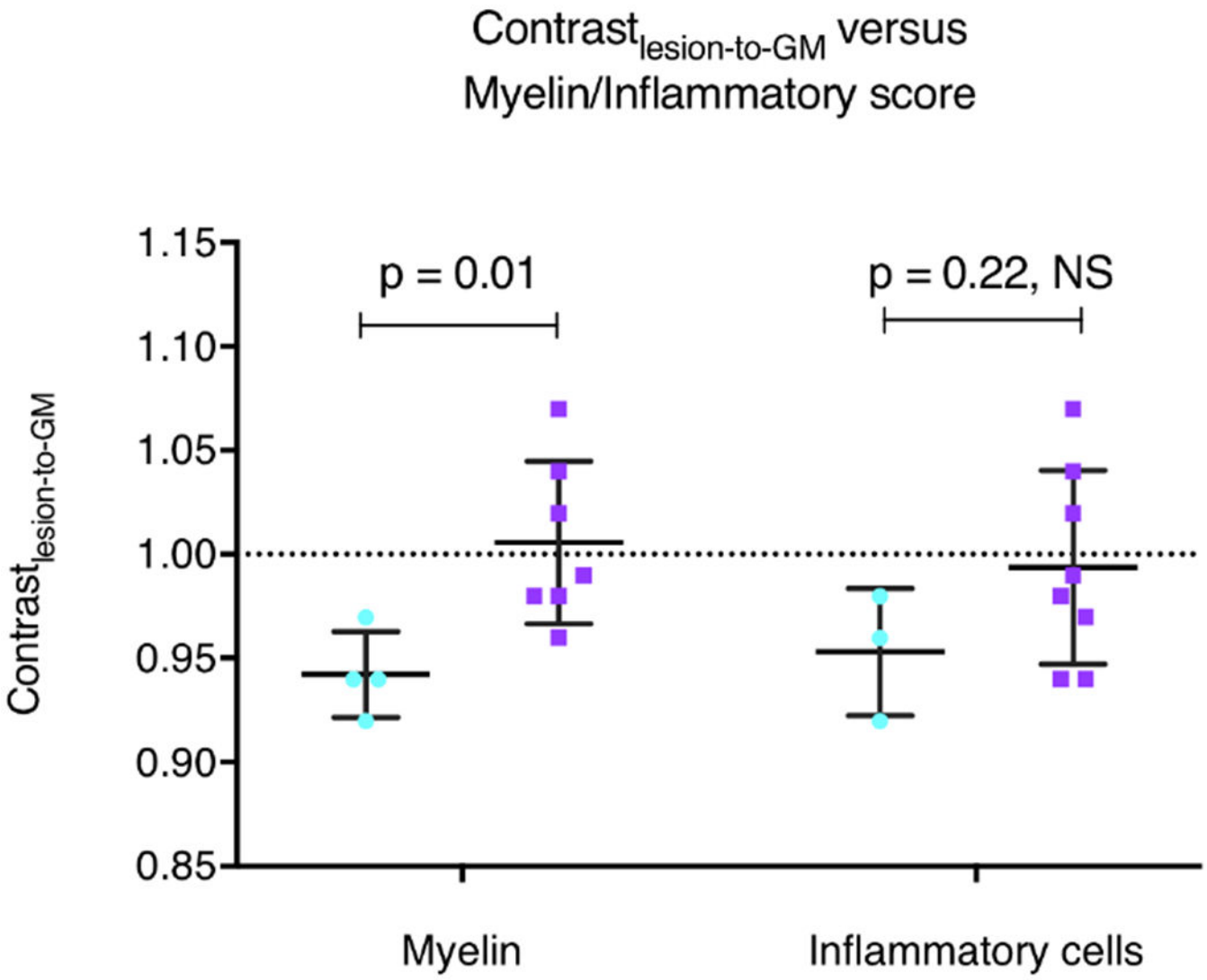

Figure 4.

Contrast$_{\text{lesion-to-GM}}$ values for each white matter lesion (n=11) grouped according to histopathological scores for myelin and inflammatory cells (light blue: score = 1; purple: score = 2).

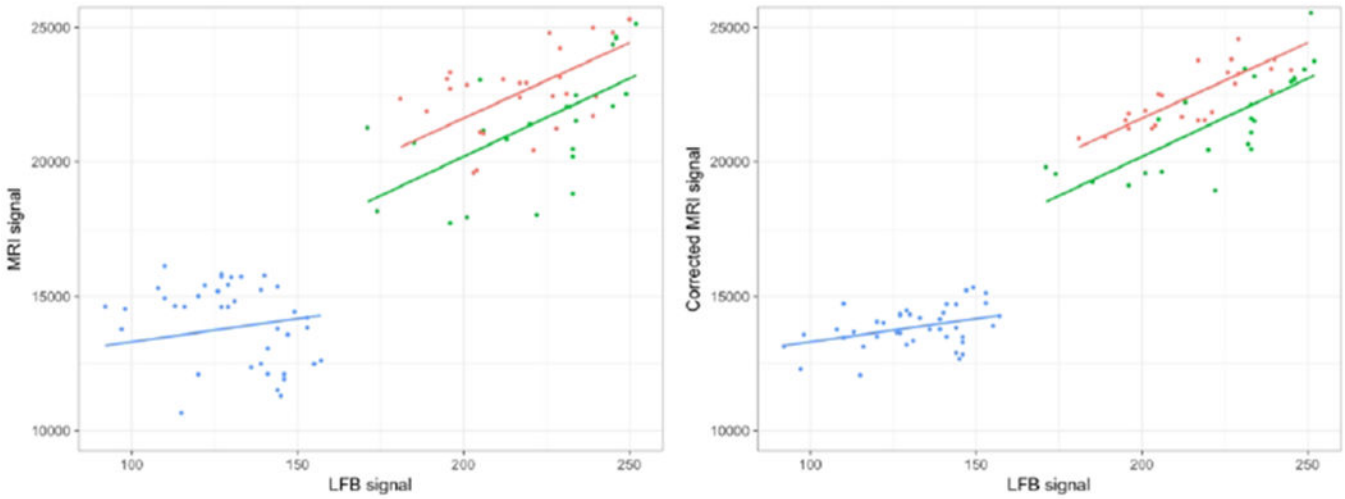

Figure 5.

Left: relationship between the observed MRI signal intensity values and LFB signal intensity using myelin model M_2. Each dot represents the individual ROI values according to their tissue type. The fitted line represents the estimated MRI values for fixed effect only. Right: representation of the random effect correction on the MRI value estimations. The corrected MRI signal was obtained by removing the estimated random effect value from the mixed effect model for each section. The residual variation, which is neither explained by fixed effect nor random effect, is shown by the distance between the individual dot and its corresponding value within the fitted line. Green: lesion; red: gray matter; blue: NAWM.

Table 1:

Demographic and clinical information of the five marmosets included in this study.

Animal	Immunization	Sex	Age (years)	Disease duration (days)	EAE score at termination	Clinical symptoms
M#1	WMH	M	3.6	134	3	Weight loss, lethargy, ataxia, severe weakness, sensory loss, vision loss
M#2	WMH	F	4.6	159	3	Apathy, tetraparesis, sensory loss, vision loss
M#3	WMH	F	2.9	123	N/A	N/A
M#4	WMH	F	1.5	89	N/A	N/A
M#5	None	F	4.9	-	-	-

Table subheading: Note that clinical information for M#3 and M#4 were not tracked over the course of the disease. Disease duration is measured as time from immunization to termination. EAE scores are defined in Kap YS et al., 2008[4]. WMH: white matter homogenate, M: male, F: female, N/A: not available.

Table 2:

Summary of the different regression models applied to the data with their respective Akaike information criteria results for the different myelin models (using the LFB-PAS histology) and inflammation models (using the Iba-1).

Models	Dependent Variable	Fixed-Effects	Interaction Term	Random Effect	Myelin model		Inflammation model	
					AIC	ΔAIC	AIC	ΔAIC
M_0	MRI	Histopathology, tissue type	No	No	1640.6	91.6	1618.4	20.1
M_1	MRI	Histopathology, tissue type	No	Section	1557.8	8.8	1598.3	0
M_2	MRI	Histopathology, tissue type	Yes	Section	1549	0	1599.3	1

Table subheading: AIC: Akaike information criteria

Table 3:

Characterization of the focal lesions by spinal cord level, size, and white matter location in the four marmosets with EAE.

	Animal	M#1	M#2	M#3	M#4	Average across marmosets
Number of focal WM lesions by cord level	cervical	11	5	10	8	8.5
	thoracic	9	10	10	11	10
	lumbar	1	2	5	3	2.8
Number of focal lesions classified by size and corresponding average volume [STD] in mm^3	small	10 ; 0.025 [0.013]	9 ; 0.033 [0.014]	21 ; 0.028 [0.009]	17 ; 0.026 [0.013]	14 ; 0.028 [0.01]
	medium	9 ; 0.14 [0.1]	8 ; 0.13 [0.089]	2 ; 0.078 [0.003]	5 ; 0.086 [0.022]	6 ; 0.12 [0.08]
	large	2 ; 4.18 [0.59]	0	2 ; 0.9 [0.68]	0	1 ; 2.54 [1.96]
Number of focal WM lesions by location	Posterior	9	1	3	2	3.8
	Left lateral	8	10	20	10	6.9
	Right lateral	3	6	2	10	5.3
	Anterior	1	0	0	0	0.25

Table subheading: WM: white matter; STD: standard deviation

Table 4:

Characterization of the subpial lesions as a percentage of the total white matter for selected spinal levels in the four marmosets with EAE.

	Animal	M#1	M#2	M#3	M#4	Average across marmosets
Relative thickness (% of white matter) of subpial lesions by cord level	Cervical C7	18	15	5	30	17
	Thoracic T7	16	20	11	54	25
	Lumbar L3	19	14	10	39	21